

# PREDICTING STELLAR-MASS BLACK HOLE POPULATIONS IN GLOBULAR CLUSTERS

NEWLIN C. WEATHERFORD,<sup>1</sup> SOURAV CHATTERJEE,<sup>1</sup> CARL L. RODRIGUEZ,<sup>1,2</sup> AND FREDERIC A. RASIO<sup>1</sup>

<sup>1</sup>*Center for Interdisciplinary Exploration & Research in Astrophysics (CIERA)  
Physics and Astronomy, Northwestern University, IL 60202, USA*

<sup>2</sup>*MIT-Kavli Institute for Astrophysics and Space Research, 77 Massachusetts Avenue, 37-664H, Cambridge, MA 02139, USA*

## ABSTRACT

Recent discoveries of black hole (BH) candidates in Galactic and extragalactic globular clusters (GCs) have ignited interest in understanding how BHs dynamically evolve in a GC and the number of BHs ( $N_{\text{BH}}$ ) that may still be retained by today's GCs. Numerical models show that even if stellar-mass BHs are retained in today's GCs, they are typically in configurations that are not directly detectable. We show that a suitably defined measure of mass segregation ( $\Delta$ ) between, e.g., giants and low-mass main-sequence stars, can be an effective probe to indirectly estimate  $N_{\text{BH}}$  in a GC aided by calibrations from numerical models. Using numerical models including all relevant physics we first show that  $N_{\text{BH}}$  is strongly anticorrelated with  $\Delta$  between giant stars and low-mass main-sequence stars. We apply the distributions of  $\Delta$  vs  $N_{\text{BH}}$  obtained from models to three Milky Way GCs to predict the  $N_{\text{BH}}$  retained by them at present. We calculate  $\Delta$  using the publicly available ACS survey data for 47 Tuc, M 10, and M 22, all with identified stellar-mass BH candidates. Using these measured  $\Delta$  and distributions of  $\Delta$  vs  $N_{\text{BH}}$  from models as calibration we predict distributions for  $N_{\text{BH}}$  expected to be retained in these GCs. For 47 Tuc, M 10, and M 22 our predicted distributions peak at  $N_{\text{BH}} \approx 8, 15$ , and 40, whereas, within the  $2\sigma$  confidence level,  $N_{\text{BH}}$  can be up to  $\sim 100, 50$ , and 200, respectively.

*Keywords:* methods: numerical-methods: statistical-stars: black holes-stars: kinematics and dynamics-globular clusters: general-globular clusters: individual (47 Tuc, M 10, M 22)

## 1. INTRODUCTION

Recent discoveries of black hole (BH) candidates in Galactic and extragalactic globular clusters (GCs; [Maccarone et al. 2007](#); [Chomiuk et al. 2013](#); [Strader et al. 2012a](#); [Miller-Jones et al. 2015](#)) have dramatically altered the traditional belief that GCs do not presently retain more than a few stellar-mass BHs (e.g., [Spitzer 1969](#)). Traditionally, it was believed that BHs, followed by mass-segregation create a high-density and low- $N$  subcluster at the center of the host cluster. Frequent and energetic dynamical encounters in this BH-subcluster eject most BHs on a few Gyr timescale (e.g., [Kulkarni et al. 1993](#); [Sigurdsson & Hernquist 1993](#); [Portegies Zwart & McMillan 2000](#)). Thus the GCs, being typically  $\sim 12$  Gyr old, were expected to retain at most a couple of BHs at present. However, modern state-of-the-art simulations of massive star clusters indicate that BHs, unless ejected from the clusters due to natal kicks, actually have a much longer evaporation timescale than was previously believed. Theoretically, this is because most BHs do not stay dynamically decoupled from the rest of the cluster for any prolonged period of time, as was assumed in past rate-based studies (e.g., [Breen & Heggie 2013](#); [Morscher et al. 2013, 2015](#); [Chatterjee et al. 2017b](#)). These simulations also suggest that the binary fraction in BHs typically remains low, both with BH and non-BH companions (e.g., [Morscher et al. 2015](#); [Chatterjee et al. 2017b](#)). In addition, due to the low duty cycles for the active state of a mass-transferring BH (e.g., [Kalogera et al. 2004](#)), it was suggested that finding even a handful of mass-transferring BH candidates via X-ray and radio emissions likely indicates a much larger population of undetected retained BHs in these clusters (e.g., [Umbreit 2012](#)).

The discovery of gravitational waves (GW) emitted from merging binary black holes (BBHs) by the LIGO/Virgo collaboration has reignited interest in understanding the astrophysical origins of BBHs (e.g., [Abbott et al. 2016a,b,c,d, 2017](#)). It has been shown by several groups that high-mass and dense star clusters, such as the GCs, can be hotbeds for the dynamical production of BBHs that would merge in the local universe and be detected by LIGO, Virgo, and LISA (e.g., [Banerjee et al. 2010](#); [Rodriguez et al. 2015](#); [Antonini et al. 2016](#); [Rodriguez et al. 2016a,b](#); [Chatterjee et al. 2017b,a](#); [Askar et al. 2017](#)). Current rate analysis indicates that this dynamical formation channel may account for at least half of all BBH mergers LIGO will detect (e.g., [Rodriguez et al. 2016a](#)). The retention fraction of BHs as a function of time not only affects the dynamical formation rate of BBHs, the energetic encounters involving BHs also can dramatically alter the overall evolution, and even long-term survival, of the host clusters (e.g., [Chatterjee et al. 2017b](#)). Thus the long-term retention and dynamical evolution of BHs in massive and dense

star clusters is of great interest for several branches of astrophysics.

While it is beyond doubt that massive star clusters form a large number of BHs,  $\sim 10^{-3}N$ , where  $N$  is the initial number of stars, e.g., assuming the initial stellar mass function (IMF) given by [Kroupa 2001](#), how long they remain bound to the clusters and take part in the internal dynamics depends on several assumptions that lack strong observational constraints, including major ones such as the distribution of natal kicks the BHs receive and the mass function of BHs at birth. GCs in the Milky Way (MW) provide a unique laboratory to test the long-term retention of BHs in high-mass, high-density, and old star clusters, shown to be ideal for the creation of high-mass BBHs merging in the local universe.

Observationally inferring the existence of a large population of retained BHs in a GC, however, is not straightforward. Although it was initially suggested that a GC hosting a BH candidate likely hosts a large number of undetected BHs (e.g., [Umbreit 2012](#)), results from modern simulations suggest that the number of mass-transferring BHs in a GC at any given time is not correlated with the total number of BHs ( $N_{\text{BH}}$ ) retained in that GC ([Chatterjee et al. 2017a](#); [Kremer et al. 2017](#)) at the time. Interestingly, the GCs that host the discovered BH candidates also do not show any apparent trends or specialty in their easily observable global properties such as the core radius, concentration, and mass (e.g., [Chomiuk et al. 2013](#); [Strader et al. 2012a](#); [Miller-Jones et al. 2015](#)). Hence, contrary to the initial expectations, detection of a mass-transferring BH candidate does not necessarily indicate the existence of a large population of undetected BHs in that cluster. Simulations also show that it is hard to infer the existence of a large population of BHs simply from the observed structural profile of a GC since the BH-mediated dynamics typically leave little signature in the observed light profile of the overall cluster, apart from making the cluster appear puffier (e.g., [Chatterjee et al. 2017a](#)).

BHs affect the overall evolution of a GC primarily through mass-segregation. Via gravitational encounters lighter stars typically gain energy and heavier stars lose energy. As a result, the heavier stars sink into the gravitational potential of a cluster on a timescale proportional to the product of the local relaxation time and the ratio of the average mass of nearby stellar species to the mass of the heavier stars (e.g., [King et al. 1995](#); [Gürkan et al. 2004](#)). GCs typically are older than their relaxation times, so they are expected to be mass segregated. The resultant mass segregation is driven by the most massive species in a cluster at any given time. Hence, while a large number of BHs are still present, they dominate the central part of a GC and drive lower-mass stellar species outward. While the BHs cannot be observed directly, bright stars from different mass

ranges are observable and their relative locations can be compared. Since the degree of mass segregation is directly related to the internal dynamical evolution of all stellar species, bright or dark, several groups have proposed that this can be used to infer the existence of hard-to-observe dark remnants in a GC. In particular, a dynamically significant dark population at the center of a GC quenches the level of mass segregation ( $\Delta$ ) between bright stars of different mass ranges. For this reason, using  $\Delta$  to infer the existence of an intermediate-mass BH (IMBH) at the center of a GC was proposed more than a decade ago (e.g., Baumgardt et al. 2004; Trenti et al. 2007). More recently, this measure has been used to put upper limits on the mass of an IMBH in real clusters by Pasquato et al. 2016. Using timescale arguments and somewhat idealized treatments of BH retention, Peuten et al. (2016) suggested that the lack of mass-segregation between the blue straggler stars (BSs) and stars near the main-sequence turn-off (MSTO) in NGC 6101 may be due to an undetected population of retained BHs. Alessandrini et al. (2016) also showed that the number of retained dark remnants can quench mass segregation between BSs and a set of lower-mass reference stars.

Our goal in this study is to construct an ‘observer-friendly’ mass segregation parameter that can be easily used independent of the GC. In general, to quantify mass segregation, one must define two stellar populations different in their typical masses and construct a measure of the difference in their radial locations. Using BSs to construct the heavier visible population, similar to some of the above-mentioned studies, has some shortcomings. For example, BSs are typically low in number. Especially, production of BSs is expected to be quenched due to the presence of a large BH population in a cluster (Sigurdsson & Hernquist 1993). Production efficiency of BSs also varies among specific clusters depending on several initial cluster properties (e.g., binary fraction, central density) and internal dynamics (e.g., recently Leigh et al. 2007; Chatterjee et al. 2013a; Sills et al. 2013). Moreover, today’s BSs, by definition, had their masses changed at some unconstrained earlier epoch (e.g., Lombardi et al. 1995, 1996, 2002; Sills et al. 1997, 2001; Chen & Han 2009), which makes it harder to understand their mass segregation. Observationally, identifying BSs requires complicated and sometimes ad-hoc cuts on the color-magnitude diagram (CMD) primarily dependent on the width of the single and binary main-sequences. Even the shape of the CMD and thus the separation of the BSs from the main-sequence is filter-dependent (e.g., Dalessandro et al. 2013).

In order to avoid all of the above difficulties, we simply define the two populations as follows. We use the giant stars to represent the heavier population. We use low-mass main-sequence stars populating a particular region in the CMD defined relative to the magnitude of the MSTO to constitute the lighter population. Since both populations are anchored to the MSTO in the CMD, the

population definitions are simpler to implement consistently and can easily be adjusted for specific clusters. Additional advantages are that the number of stars in both sets are large and that the majority of the members in both sets are simple, undisturbed stars – i.e., their stellar properties are not affected by the internal dynamics of the cluster, but their radial locations are affected by the overall dynamics.

We use a large grid of state-of-the-art numerical models to relate  $\Delta$  calculated using giants and low-mass main-sequence stars to  $N_{\text{BH}}$  retained in these models. We show that measuring  $\Delta$  between giants and low-mass main-sequence (MS) stars indeed can be used to infer  $N_{\text{BH}}$  retained in these cluster models. Calibrations connecting  $\Delta$  with  $N_{\text{BH}}$  obtained from these models are then used to infer  $N_{\text{BH}}$  in a handful of real GCs in the Milky Way (MW) using the publicly available ACS survey data (Sarajedini et al. 2007).

We describe our models and define the stellar populations used to quantify mass segregation in Section 2. We show our key results connecting  $\Delta$  with  $N_{\text{BH}}$  in our models in Section 3. In Section 4, we show how the dependence between  $\Delta$  and  $N_{\text{BH}}$  can be used for real GCs to infer the  $N_{\text{BH}}$  retained by them by selecting three GCs in the MW containing known BH candidates, and for which we can calculate  $\Delta$  using the publicly available ACS survey data (Sarajedini et al. 2007). We use the theoretically calibrated relations connecting  $N_{\text{BH}}$  and  $\Delta$  and predict the expected  $N_{\text{BH}}$  in these GCs based on the measured  $\Delta$  in Section 5. Finally, we summarize our results and conclude in Section 6.

## 2. NUMERICAL MODELS AND EXTRACTION OF MODEL PARAMETERS

We create a large grid of cluster models using our Hénon-type (Hénon 1971a,b) Cluster Monte Carlo code (CMC) that has been developed and rigorously tested over the last 17 years (Joshi et al. 2000, 2001; Fregeau et al. 2003; Fregeau & Rasio 2007; Chatterjee et al. 2010; Umbreit et al. 2012; Chatterjee et al. 2013b). For recent updates and validation of CMC see (Pattabiraman et al. 2013; Morscher et al. 2015; Rodriguez et al. 2016c).

We vary the initial model properties motivated by observational constraints from high-mass young star clusters, thought to be similar in properties for GC progenitors (e.g., Scheepmaker et al. 2007; Chatterjee et al. 2010). The initial  $N$  is between  $2 \times 10^5$  and  $2 \times 10^6$ , the metallicity ( $Z$ ) is between  $Z/Z_{\odot} = 0.005$  and 1, virial radius is between  $r_v/\text{pc} = 1$  and 2, galactocentric distance is between  $R_g/\text{kpc} = 1$  and 20, and the initial binary fraction is between  $f_b = 0.04$  and 0.1. The positions and velocities of single stars and center of mass of binaries are drawn from a King profile with concentration  $w_0 = 5$  (King 1966). Stellar masses (primary mass in case of a binary) are drawn from the IMF for star clusters given in Kroupa (2001) between 0.08 and  $150 M_{\odot}$ . Binaries are assigned by randomly choosing

$N \times f_b$  stars independent of radial position and mass and assigning a secondary adopting a uniform mass ratio ( $q$ ) between  $0.08/m_p$  and 1, where  $m_p$  denotes the primary mass. Binary periods are flat in log intervals and eccentricities are thermal. We include all relevant physical processes, such as two-body relaxation, strong binary-mediated scattering, and galactic tides. Single and binary stellar evolution is followed using SSE and BSE packages (Hurley et al. 2000, 2002) updated to include our latest understanding on stellar winds (e.g., Vink et al. 2001; Belczynski et al. 2010) and BH formation physics (e.g., Fryer et al. 2012). Finally, to ensure that our results are not affected by clusters close to dissolution – at that point, the assumption of spherical symmetry in CMC is incorrect – only models that reached 12 Gyr while retaining  $\geq 30\%$  of their initial  $N$  were included in the analysis. In total, we use 37 different combinations of initial properties and a total of 153 separate models including multiple realizations of models using the same combination of initial properties. Detailed descriptions of each model are given in Table 1.

### 2.1. “Observing” Model Clusters

CMC periodically generates the dynamical and stellar properties of all single and binary stars including the luminosity ( $L$ ), temperature ( $T$ ), and radial positions. We assume spherical symmetry and project the radial positions of all single and binary stars in two-dimensions to create sky-projected snapshots of the cluster models at different times. Taking into account the typical age range of MWGCs, we use up to 4 snapshots for each model realization, corresponding roughly to  $t = 9, 10, 11$ , and 12 Gyr. In some model realizations, CMC did not output a snapshot near enough to all 4 of these standardized ages (within 0.25 Gyr). Such realizations therefore contributed fewer than 4 snapshots to the analysis. The number of snapshots used in our analysis is included for each model in Table 1 for reference. In total, we use 554 snapshots. For each single star we calculate the  $T$  from  $L$  and the stellar radius  $R$  (given by BSE) assuming black-body. All binaries are treated as unresolved sources. In case of a binary, we use the total luminosity  $L = L_1 + L_2$  and a  $L$ -weighted temperature given by

$$T_{\text{eff}} = \frac{T_1 L_1 + T_2 L_2}{L_1 + L_2} \quad (1)$$

We account for statistical fluctuations by performing 50 realizations of 2D projections for each snapshot selected as above by varying the random seed. For each realization of the 2D-projected snapshots we calculate the core radius ( $r_{c,\text{obs}}$ ) and the central surface luminosity density ( $\Sigma_{c,\text{obs}}$ ) by fitting an analytic approximation of the King model (Eq. 18; King 1962) to the cumulative luminosity profile (e.g., Chatterjee et al. 2017b). We also calculate the half-light radius ( $r_{\text{hl}}$ ) as the sky-projected distance from the center within which half of the total cluster light is contained.

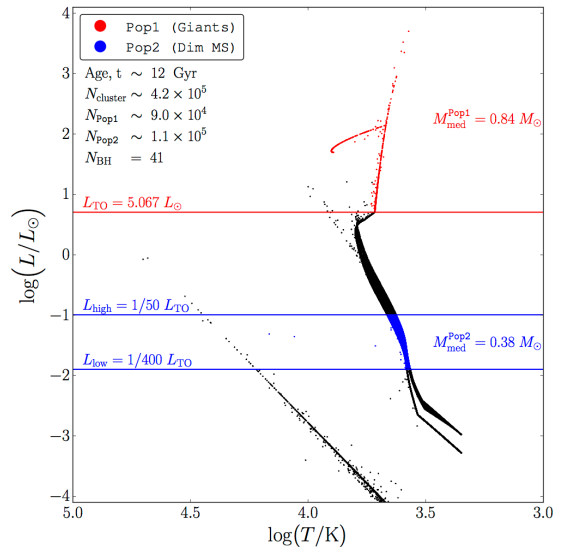


**Figure 1.** Example Hertzsprung-Russell Diagram (HRD) from a model at  $t = 12$  Gyr (model no. 6; Table 1) showing the two stellar populations compared for measuring the level of mass segregation. Each dot represents a single or binary star (all binaries are considered unresolved). Red and blue denote our high-mass (Pop1) and low-mas (Pop2) populations, respectively. Each population is defined with respect to the luminosity at the MSTO (boundaries are shown in the figure). The median masses for Pop1 and Pop2 are also shown in the figure. Relevant cluster properties at the time of this snapshot such as  $N$ ,  $N_{\text{BH}}$ , and the respective numbers in each stellar population ( $N_{\text{Pop1}}$  and  $N_{\text{Pop2}}$ ) are also shown in the figure. Stellar populations defined this way ensures high number of stars in each population.

### 2.2. Population Selection

In general, quantifying  $\Delta$  in a GC requires comparison between the radial distributions of multiple stellar populations sufficiently different in their average masses (e.g., Goldsbury et al. 2013). However, mass is not directly measured in real clusters – stellar luminosities are, and can be used as a proxy for mass, especially in the MS (e.g., Hansen & Kawaler 1994). While any two populations sufficiently different in their average masses could work for our study, devising a recipe that can be applied consistently to numerical models as well as most real GCs is somewhat challenging and to some degree a matter of choice. To ascertain maximum signal strength the two populations must have characteristic masses as different as possible, but at the same time, the lighter population must not be so faint that they are hard to observe in a real GC. In addition, both populations must contain large enough numbers of stars to limit statistical scatter. We decide to anchor the definitions of the two populations to the location of the MSTO on a CMD, the most prominent feature on any CMD. The giants are used as the heavier population, henceforth called Pop1.

**Table 1.** Initial Properties of Cluster Models

Model	Runs	Snapshots	$r_v/\text{pc}$	$Z/Z_\odot$	$R_g/\text{kpc}$	$N$	$f_b$
1	9	36	1	0.01	20	2e5	10
2	5	20	1	0.01	20	5e5	10
3	2	8	1	0.01	20	1e6	10
4	2	8	1	0.01	20	2e6	10
5	12	48	1	0.05	8	2e5	10
6	5	20	1	0.05	8	5e5	10
7	6	20	1	0.05	8	8e5	10
8	2	8	1	0.05	8	1e6	10
9	2	8	1	0.05	8	2e6	10
10	5	20	1	0.25	2	5e5	10
11	2	8	1	0.25	2	1e6	10
12	2	8	1	0.25	2	2e6	10
13*	4	12	2	0.005	8	8e5	10
14	10	36	2	0.01	20	2e5	10
15	5	20	2	0.01	20	5e5	10
16	2	8	2	0.01	20	1e6	10
17	2	8	2	0.01	20	2e6	10
18	1	4	2	0.015	20	8e5	5
19	8	26	2	0.025	8	8e5	10
20	6	14	2	0.05	8	2e5	10
21	13	50	2	0.05	8	2e5	10
22	5	20	2	0.05	8	5e5	10
23	2	8	2	0.05	8	1e6	10
24	2	8	2	0.05	8	2e6	10
25	1	4	2	0.05	8	8e5	4
26	2	8	2	0.05	8	8e5	5
27	5	17	2	0.05	8	8e5	10
28	1	4	2	0.15	4	8e5	5
29	3	12	2	0.25	2	5e5	10
30	2	8	2	0.25	2	1e6	10
31	2	8	2	0.25	2	2e6	10
32	5	16	2	0.25	8	8e5	10
33	1	4	2	0.35	2	8e5	5
34*	8	21	2	0.5	8	8e5	10
35*	4	11	2	0.75	8	8e5	10
36*	4	11	2	1.0	8	8e5	10
37*	1	4	2	1.0	1	8e5	5

NOTE—‘Model’ denotes cluster models with a particular set of initial properties. ‘Runs’ denote the number of realizations performed. ‘Snapshots’ denote the number of snapshots taken into our analysis between 9 and 12 Gyr.  $r_v$ ,  $Z$ ,  $R_g$ ,  $N$ , and  $f_b$  denote the initial virial radius, stellar metallicity, galactocentric distance, number of objects, and binary fraction, respectively. ‘\*’ denotes that these models were not used for  $\Delta-N_{\text{BH}}$  calibration because the  $Z$  of these models are not representative of the three GCs of interest in this study (Section 4).



The lighter population, Pop2, is selected to be the MS stars with  $L_{\text{TO}}/400 \leq L \leq L_{\text{TO}}/50$ , where  $L_{\text{TO}}$  is the luminosity at MSTO on a Hertzsprung-Russel Diagram (HRD) (Figure 1). The limits in  $L$  for Pop2 are chosen to optimize the signal strength for mass segregation while making sure that the equivalent area on a CMD for real GCs is available from the ACS GC survey (Sarajedini et al. 2007) for the GCs of interest. In our models at  $t = 12$  Gyr we find that the median masses in Pop1 and Pop2 are 0.84 and 0.34, respectively. The ranges in masses overlap marginally due to the binaries in Pop2. GCs are old stellar populations with a small range in ages. Thus, defining the two populations based on the  $L_{\text{TO}}$  also ensures that very similar mass ranges are selected in the populations independent of the model. In addition, for real GCs, it is trivial to transfer these definitions to any magnitude system simply remembering the conversion from  $L$  to magnitude. These benefits will be apparent when we consider real GCs (Section 4).

We want to mention that other populations could be compared as well. For example, recent studies (Peuten et al. 2016; Alessandrini et al. 2016) have used BSs and stars on the upper MS as two populations. Both populations are luminous and BSs are expected to be more massive than stars on the MS. However, while these choices are sufficient to demonstrate the anti-correlation between mass segregation and  $N_{\text{BH}}$ , stochastic noise due to the small size of the BS population can limit the accuracy of any measurement of  $\Delta$ , especially since it is also expected that high BH retention should decrease BS formation efficiency (e.g., Sigurdsson & Hernquist 1993). In contrast, giants and low-mass MS stars are both plentiful in a typical GC. As an example, the model represented in Figure 1 (model no. 6 in Table 1) at  $t = 12$  Gyr contains  $\sim 9 \times 10^4$ ,  $\sim 10^5$ , and  $\approx 36$  Pop1 Pop2, and BSs, respectively. In addition, BSs by definition changed mass at some unknown past epoch, whereas, the majority of both populations are normal, undisturbed stars. Hence, mass segregation between giants and low-mass MS stars is easier to interpret compared to populations involving BSs.

### 2.3. Quantifying Mass Segregation

Having chosen two distinct populations, we now define two similar methods for quantifying  $\Delta$  between Pop1 and Pop2 using the cumulative distribution functions (CDF) of the 2D projected cluster-centric positions (Figure 2). Our fiducial parameter is defined to be the difference between the projected cluster-centric distances at the medians of the two cumulative distributions described above, normalized by the  $r_{\text{hl}}$ :

$$\Delta_{r50} = \frac{r_{50,2} - r_{50,1}}{r_{\text{hl}}}. \quad (2)$$

Here,  $r_{50,i}$  denotes the median of the CDF for the projected locations of the  $i^{\text{th}}$  population.

Simply to ensure that our results are not sensitive to the exact definition of  $\Delta$ , we adopt another equivalent definition following Alessandrini et al. (2016), namely, the normalized area between the CDFs for the two populations:

$$\begin{aligned} \Delta_A &= \int_{r_{\text{min}}}^{r_{\text{max}}} \frac{dr}{r_{\text{hl}}} \left[ f_1\left(\frac{r}{r_{\text{hl}}}\right) - f_2\left(\frac{r}{r_{\text{hl}}}\right) \right] \\ &= \frac{A_1 - A_2}{r_{\text{hl}}}. \end{aligned} \quad (3)$$

Here, the integration is performed over the full range in projected cluster-centric distances,  $f_i$  denotes the CDF for population  $i$ , and  $A_i$  denotes the area under  $f_i$ .

While  $\Delta_A$  samples all parts of the CDFs and may be more robust especially when one of the populations does not contain a large enough number of stars, we find that in our models and our stellar populations,  $\Delta_{r50}$  and  $\Delta_A$  show little difference in precision and level of fluctuations between realizations (for the 2D projections). Hence, while we present both  $\Delta_A$  and  $\Delta_{r50}$  for all our models in Table 3, we show the simpler-to-compute  $\Delta_{r50}$  in subsequent figures. Note that the same figures could also be made for  $\Delta_A$  and they would show essentially identical correlations.

## 3. NUMBER OF BLACK HOLES AND MASS SEGREGATION: MODELS

In this section we study the correlation between  $N_{\text{BH}}$  in a model cluster and  $\Delta$  measured using Pop1 and Pop2 stars in that model (Section 2.2; Figure 3). Note that in terms of causality, retention of BHs lead to quenching of  $\Delta$ . However, since  $\Delta$  can be measured in a real GC, and our goal is to infer  $N_{\text{BH}}$  from  $\Delta$ , we treat  $\Delta$  as the independent variable and  $N_{\text{BH}}$ , normalized by the total number of cluster stars, as the dependent variable. Figure 3 contains results from a total of 27,700 independent realizations of sky-projected clusters. Each data point corresponds to a snapshot of an independent model between 9 and 12 Gyr. The markers and error bars denote the median and standard deviation based on 50 independent 2D projections performed on each snapshot.

Several interesting trends emerge. Both measures of mass segregation,  $\Delta_{r50}$  and  $\Delta_A$ , show the same strong anti-correlation with  $N_{\text{BH}}/N_{\text{cluster}}$ , i.e., the higher the  $N_{\text{BH}}/N_{\text{cluster}}$ , the lower the  $\Delta$ . On top of this general trend, there is also an apparent trend dependent on the stellar metallicity. The higher the  $Z$ , the lower the mass of the BHs produced. As a result, to quench  $\Delta$  to the same level, a higher- $Z$  cluster needs higher  $N_{\text{BH}}/N_{\text{cluster}}$  compared to a lower- $Z$  cluster. Other parameters such as the initial binary fraction  $f_b$ , natal kick distribution, and cluster age contribute to the spread in the observed trend and can be marginalized in the overall calibration involving only  $\Delta$  and  $N_{\text{BH}}/N_{\text{cluster}}$ . For example, a higher natal kick distribution simply ejects more BHs

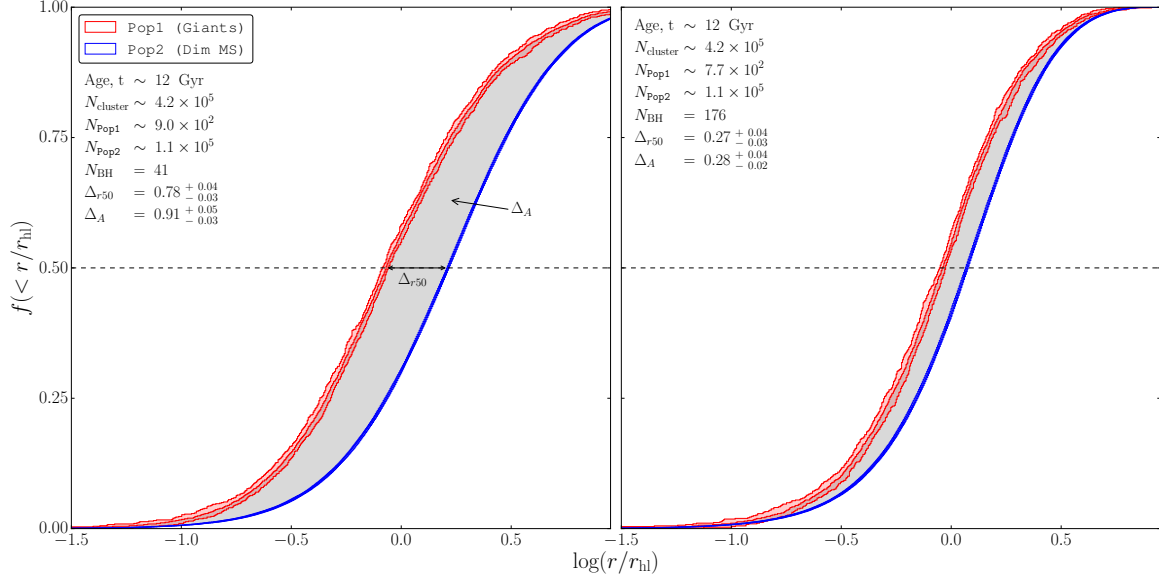


**Figure 2.** Example cumulative distributions for the projected radial locations in the cluster for **Pop1** and **Pop2** objects (single and binary stars; Section 2.2). Left and right panels show examples from clusters containing 41 and 176 BHs at  $t = 12$  Gyr (models no. 6 and 22; Table 1). Red and blue histograms denote **Pop1** and **Pop2**, respectively. In each case, the red and blue shaded regions denote the range in statistical fluctuations based on 50 realizations of 2D projections for the same radial distribution of stars in the cluster. Clearly, the higher-mass population **Pop1** is more centrally concentrated than the lower-mass population **Pop2**. The measure of mass segregation ( $\Delta_{r50}$  or  $\Delta_A$ ) between **Pop1** and **Pop2** depend on the number of retained BHs. For example, the model cluster shown in the right panel containing a larger  $N_{\text{BH}}$  shows a clear quenching of  $\Delta$  between **Pop1** and **Pop2** relative to the cluster shown in the left panel containing fewer  $N_{\text{BH}}$ .

from the cluster at birth, leading to a lower  $N_{\text{BH}}/N_{\text{cluster}}$  at a later time  $t \geq 9$  Gyr. Similarly, variations in  $f_b$  slightly modify the relative masses of the visible populations and those of the retained BHs (typically single due to frequent dynamical encounters, wind mass loss, and supernova; e.g., Chatterjee et al. 2017b) and contribute to the spread in the anti-correlation between  $N_{\text{BH}}/N_{\text{cluster}}$  and  $\Delta$ .

Note that statistical fluctuations due to independent projections of the snapshots are of similar magnitude for both  $\Delta_{r50}$  and  $\Delta_A$ . This ensures that fluctuations in the measure of mass-segregation are realistic and depend simply on the viewing angle to a particular cluster. These fluctuations are not due to lack of robustness in our defined measure of mass segregation. This is only expected, since both our defined stellar populations contain a sufficiently large number of stars, and as a result, their CDFs do not suffer from noise arising from small numbers.

These models now give us the power to create a statistical calibration relating  $\Delta$  ( $\Delta_{r50}$  or  $\Delta_A$ ) to  $N_{\text{BH}}/N_{\text{cluster}}$  in real clusters. Note that in our definitions, both quantities of interest,  $N_{\text{BH}}/N_{\text{cluster}}$  and  $\Delta$ , are dimensionless. Moreover, the former and latter relate to a real cluster through the total mass and the half-light radius, both of which are easily observable within some uncertainties related to the mass-to-light ratio. To properly consider the large realistic spreads

in the parameter space depending on the cluster initial properties, we use a non-parametric gaussian kernel density estimation (KDE) to represent the probability distribution function (PDF) in the  $\Delta_{r50}-N_{\text{BH}}/N_{\text{cluster}}$  (alternatively,  $\Delta_A-N_{\text{BH}}/N_{\text{cluster}}$ ) plane instead of a deterministic best-fit approach. In later sections where we use this KDE to predict  $N_{\text{BH}}/N_{\text{cluster}}$  in real clusters, we further restrict ourselves to models with  $Z$  close to that of the respective observed clusters. As we will see, in real clusters we also need to limit model results to the maximum cluster-centric distance available in the ACS survey for individual clusters.

#### 4. MEASURING MASS SEGREGATION FOR OBSERVED CLUSTERS

We now proceed to infer  $N_{\text{BH}}$  from measured  $\Delta$  in real GCs using calibrations obtained from models. We use the ACS Survey for MWGCs (Sarajedini et al. 2007) for the stellar data. Compiled using the wide-field channel of the *Hubble Space Telescope's* Advanced Camera for Surveys (ACS), this resource consists of an exhaustive catalog of stars within the central  $4' \times 4'$  of 65 MWGCs. The catalog exists as an online database of stellar coordinates and calibrated photometry in the ACS VEGA-mag system (Sirianni et al. 2005). The database may be accessed publicly at [http://www.astro.ufl.edu/~ata/public\\_hstgc](http://www.astro.ufl.edu/~ata/public_hstgc) and its construction is fully detailed in (Anderson et al. 2008). We currently limit our analysis to 47 Tuc, M 10, and M 22 – three of four known

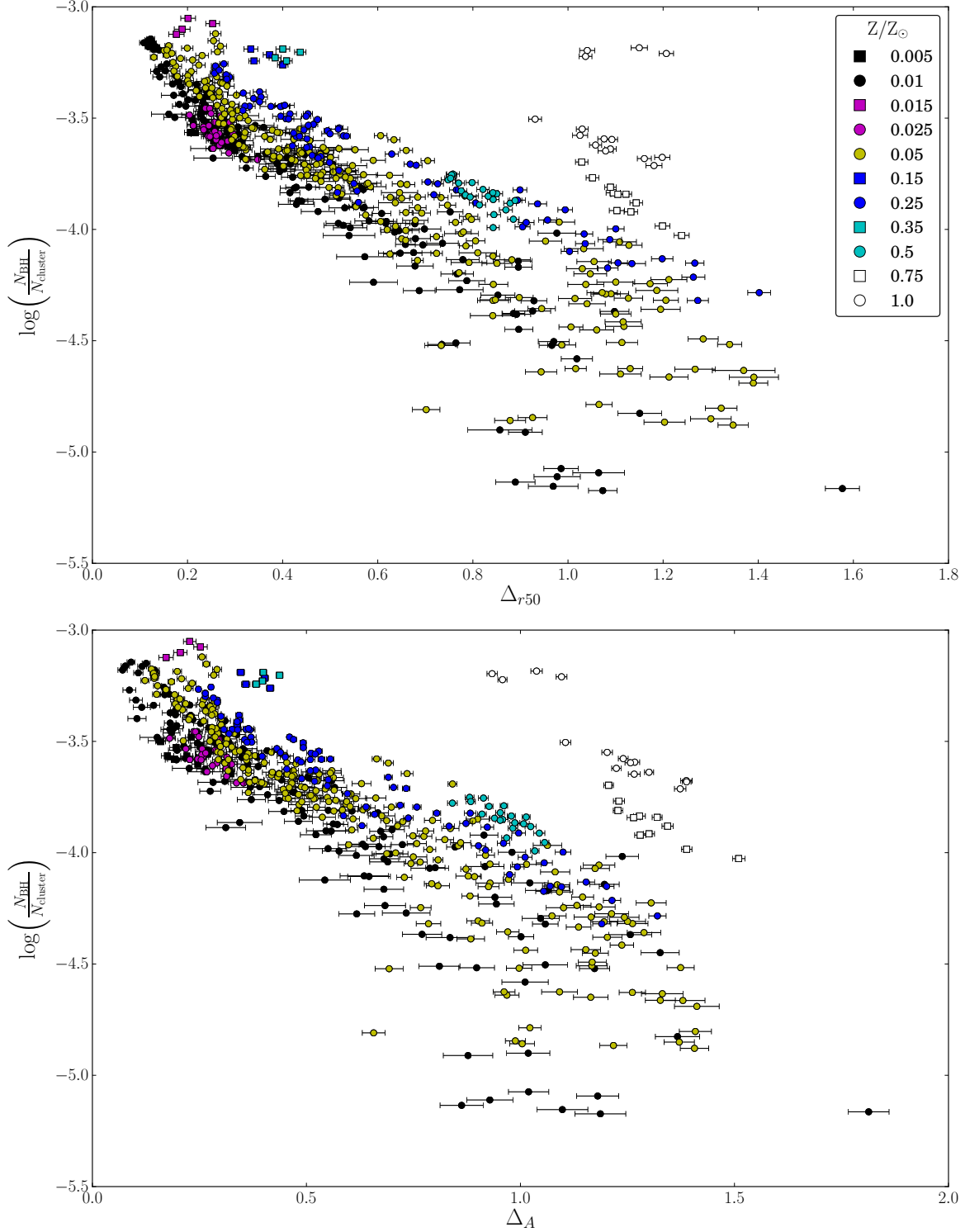


**Figure 3.** Number of retained BHs per cluster star  $N_{\text{BH}}/N_{\text{cluster}}$  vs  $\Delta_{r50}$  (top) and  $\Delta_A$  (bottom) for all model snapshots with  $t \geq 9$  Gyr (Section 2.3). Each point represents the mean of  $\Delta_{r50}$  ( $\Delta_A$ ) calculated using Eq. 2 (3) from 50 realizations of 2D projections of the radial positions of all stars in a model cluster snapshot. The error bars represent the standard deviation within these realizations. Point shape and color denote different stellar metallicities (shown in the label). A clear anticorrelation between  $N_{\text{BH}}/N_{\text{cluster}}$  and  $\Delta_{r50}$  ( $\Delta_A$ ) is apparent, especially if models of particular metallicities are considered. In addition, there is a metallicity effect: higher the metallicity, higher the  $\Delta_{r50}$  (or  $\Delta_A$ ) for any given  $N_{\text{BH}}/N_{\text{cluster}}$ . As  $Z$  increases, BH masses decrease. Thus, to affect the same level of quenching of  $\Delta$ , a higher  $N_{\text{BH}}/N_{\text{cluster}}$  is needed.



MWGCs to contain candidate stellar-mass BHs (e.g., Strader et al. 2012a; Strader 2014; Miller-Jones et al. 2015; Bahramian et al. 2017). Relevant structural properties of these three GCs are listed in Table 2 for easy reference. While M 62 also contains a stellar-mass BH candidate (e.g., Chomiuk et al. 2013), this cluster is not included in the publicly available ACS survey catalog.

In contrast to models where all relevant properties of all stars and binaries are known, analyzing real GC data is challenging in several ways. For our purposes, the most important considerations are the following. The measure of mass segregation depends on the radial limit to which stellar data is available. Because of the fixed angular size of the ACS survey, the radial extent for the available data is dependent on the heliocentric distance to the cluster. The CMD can have large scatter and the available database does not include detailed cluster-membership information. Since cluster centers are crowded fields, the completeness of stars depend on the location as well as the magnitude which can introduce biases in our measure for mass segregation. Below we describe how we analyze the ACS survey data to mitigate these challenges.

#### 4.1. ACS Field of View and Limiting Radius

Because the field of view (FOV) of the ACS only covers an approximate  $4' \times 4'$  rhombus centered on the cluster core (Figure 4), it is not possible to analyze ACS data all the way out to the tidal radius. This radial limitation on the ACS data will *reduce* the measured values of  $\Delta_{r50}$  and  $\Delta_A$  relative to those computed for the radially complete CMC models in Section 3.

The available data for each cluster of interest in this paper is shown in Figure 4. In each case the dots denote the actual stellar positions. In addition, we show the size of the observed core radius ( $r_{c,\text{obs}}$ ) and the size of the largest circle ( $r_{\text{lim}}$ ) centered at the cluster center that can be inscribed in the FOV. This allows us to only include stars up to  $r_{\text{lim}}/r_{\text{hl}} = 0.55, 0.9$ , and  $0.5$  for 47 Tuc, M 10, and M 22, respectively. In each case, we recalculate  $\Delta_{r50}$  (and  $\Delta_A$ ) for our models using the same definitions described in Section 2 but now including only stars up to a projected cluster-centric distance of  $r/r_{\text{hl,model}} = r_{\text{lim}}/r_{\text{hl}}$ . Of course, since each observed cluster has a slightly different value for  $r_{\text{lim}}/r_{\text{hl}}$ , the measure of mass segregation needs to be recalculated from models separately for each individual cluster imposing the unique radial limit. KDEs created from these custom-calculated  $\Delta_{r50}$  and  $\Delta_A$  along with  $N_{\text{BH}}/N_{\text{cluster}}$  are used to estimate the PDF for the expected retained BH number in each observed cluster.

While imposing custom radial limits similar to the observed clusters reduce the numbers of stars both in Pop1 and Pop2 in our models, the resulting increase in statistical scatter is negligible relative to the real spread in  $N_{\text{BH}}/N_{\text{cluster}}$  for any given value of  $\Delta_{r50}$  or  $\Delta_A$ . This is simply because for all radial limits imposed by the ACS

FOV, there is always a large enough number of stars in Pop1 and Pop2 as defined in Section 2.2. Still, we test the robustness of our final  $N_{\text{BH}}/N_{\text{cluster}}$  estimates by employing several smaller than necessary radial limits for M 10, the GC where  $r_{\text{lim}}/r_{\text{hl}}$  is the largest.

#### 4.2. Population Selection

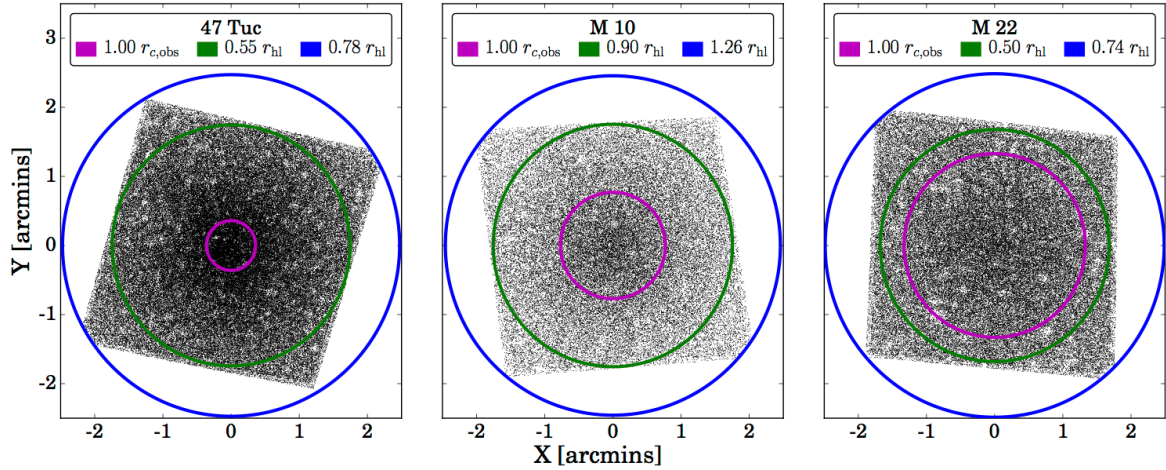
Once the radial limits are imposed, population selection proceeds as described in Section 2.2 but uses CMDs based on the ACS VEGA-mag photometric system. The two filters used in the ACS GC survey to construct CMDs are F606W (corresponding to the V-band) and F814W (corresponding to the I-band). Since our populations are defined by bounds in the CMD relative to the location of MSTO, the definitions are applicable to the GC data with any filter after a simple conversion from luminosity ratios (used in models) to magnitude ratios. We simply need to ascertain where the MSTO is for a particular cluster using those filters. In magnitudes, the 1/50th and 1/400th luminosity ratios correspond to  $m_V^{\text{TO}} + 4.247$  and  $m_V^{\text{TO}} + 6.505$ , respectively. In order to be uniform in our treatment of the ACS data, we define  $m_V^{\text{TO}}$  in the following way. We select the relevant portion of the CMD along the V-band axis that contains the turn-off – for the clusters we consider, this range is between  $m_V = 15$  and  $20$ . We split this range into 50 bins of  $0.1$ -mag width. The turnoff is then defined to be the midpoint of the bin with the lowest mean color,  $\langle m_V - m_I \rangle$ . The resulting turnoff values and low-mass population cutoffs are shown in Figure 5.

To be more conservative in our populations for real clusters we employ a further cut. The raw CMDs made from the ACS survey’s online catalog have large spreads along the MS as well as the giant branch, with several outliers (Figure 5). A sizable number of outliers have high photometric errors. Some of these stars may also simply not be cluster members. Note that for our purposes it is alright to undersample stars in both populations as long as no radial bias is introduced. Keeping this in mind we outline below how we proceed to cleanup the raw data.

The traditional process to clean up the CMD of a cluster is to employ a cut on the photometric error and measurement quality. However, as warned in (Anderson et al. 2008), cuts based strictly on the quality estimates may introduce radial biases. For example, due to crowding in regions of high stellar number density like the core, point-spread functions (PSFs) of nearby stars – especially dim neighbors to a bright giant – are not always separately resolvable. This radially biases the relative locations for giants and low-mass MS stars, essentially artificially increasing the measured  $\Delta$ . Crowding introduces another bias in photometric error. Overlapping PSFs of highly-proximate stars cannot be individually fitted as well as those in isolation. Hence, stars in the core, especially dim ones, suffer from preferentially high measurement uncertainties. Any quality

**Table 2.** Selected Properties of the GCs

Name		$M_{\text{cluster}}$	$r_{c,\text{obs}}$	$r_{\text{hl}}$	Harris Metallicity		ACS Metallicity	
NGC	Alt	$[10^5 M_{\odot}]^a$	[arcmin] <sup>b</sup>	[arcmin] <sup>b</sup>	[Fe/H] <sup>b</sup>	$Z_{\odot}$	[Fe/H] <sup>c</sup>	$Z_{\odot}$
0104	47 Tuc	7.00	0.36	3.17	-0.72	0.191	-0.78	0.166
6254	M 10	1.00	0.77	1.95	-1.56	0.0275	-1.25	0.0562
6656	M 22	2.90	1.33	3.36	-1.70	0.0200	-1.49	0.0324

<sup>a</sup> Marks & Kroupa (2010)<sup>b</sup> Harris catalog (Harris 1996, 2010 edition)<sup>c</sup> Marín-Franch et al. (2009)

**Figure 4.** Data stamps showing the fields of view for 47 Tuc (left), M 10 (middle), and M 22 (right) in the publicly available data from the ACS survey for the MWGCs (Sarajedini et al. 2007). The  $X$  and  $Y$  coordinates are obtained directly from the ACS catalog after converting the original pixel units into arcminutes (Anderson et al. 2008). Observed core radii are shown (magenta) for each GC for reference. Green circles denote the largest radial extent that can be inscribed into the data stamp for reference. For each GC, only stars contained within the green circle are considered for the calculation of mass segregation. The blue circles show the radial extent that can be superscribed to the data stamp. The observed core and half-light radii are adopted from the Harris catalog for MWGCs (Harris 1996, 2010 edition).

cut would therefore preferentially select the brighter and more isolated stars, again introducing bias leading to an artificial increase in the measured  $\Delta$ . Since the primary measurable of interest for this study is the relative radial distributions of two populations highly different in their typical magnitudes, we cannot use the above-mentioned traditional methods.

For our purposes we employ an empirical scheme based on the proximity of the stars from the nominal location of the CMD in the magnitude-color space. We first sort all stars (left panels, Figure 5) into bins of  $\delta m_V = 0.1$ . We create a PDF for the stars in each  $m_V$  bin along the color axis. We find the locations of the mode and mode-centric  $2\sigma$  limits in color for each  $m_V$  bin. For each  $m_V$  bin we exclude all stars outside the  $2\sigma$  color limits to create a cleaner version of the CMD (right panels, Figure 5). We calculate  $\Delta$  ( $\Delta_{r50}$  and  $\Delta_A$ )

using the stars in the cleaned CMD and using the same definitions of Pop1 and Pop2 stars as described above.

Note that our main goal is to ascertain that our CMD-cleaning stage does not preferentially exclude or include stars of either Pop1 or Pop2. For all of the three GCs we consider, the luminosity functions (LFs) are almost identical before and after the cleaning step, especially in the regions of our Pop1 and Pop2 for these GCs (Figure 6). This gives us confidence that the CMD cleaning stage cuts down both populations proportionally without introducing any bias in location in the cluster and  $m_V$  or  $m_V - m_I$ .

#### 4.3. Correcting for Completeness

Due to crowding, photometric completeness decreases with increasing magnitude and decreasing radial distance from the center. In other words, a dimmer stellar population will be less complete than brighter stars

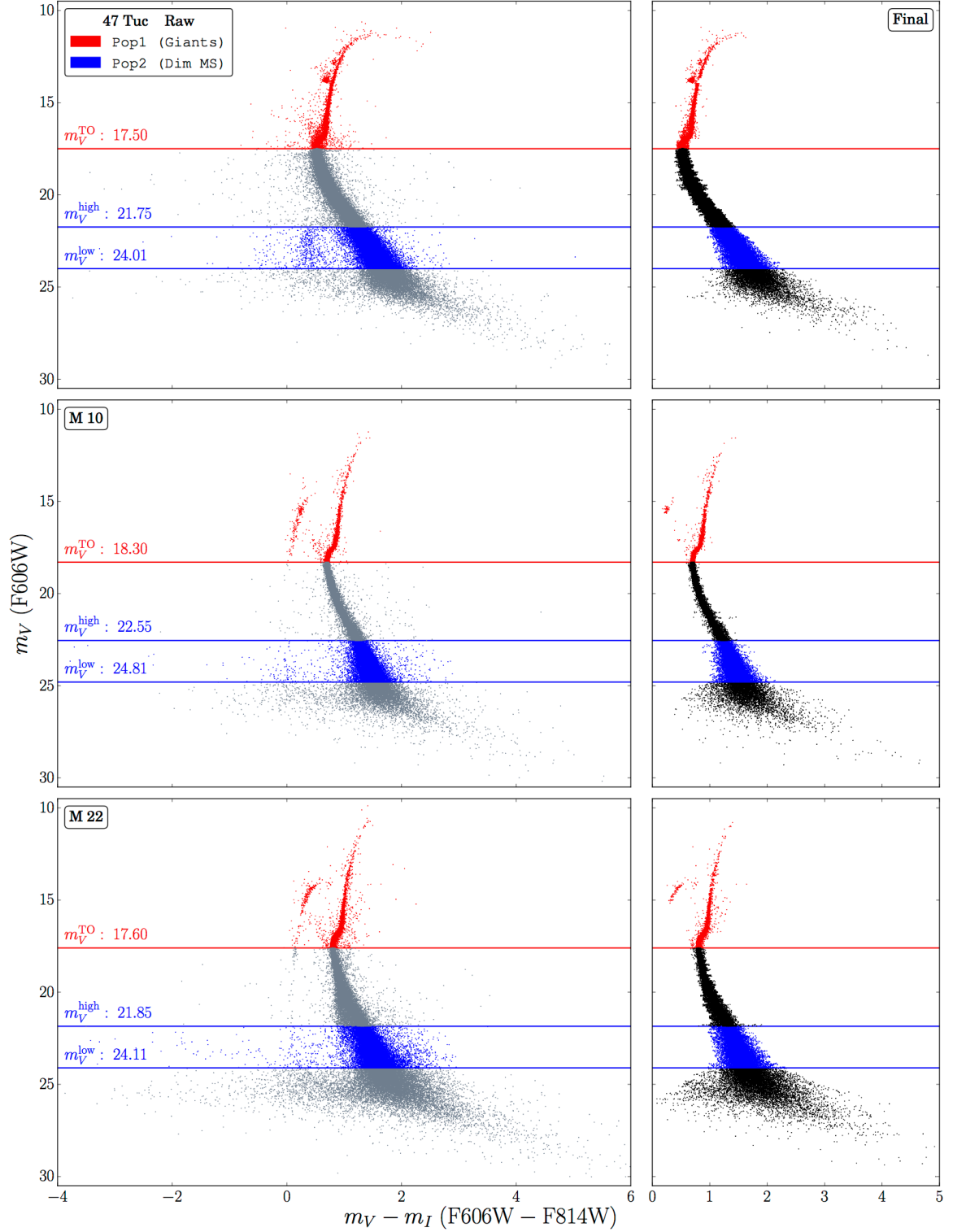


**Figure 5.** Raw (left) and cleaned (right) CMDs for 47 Tuc (top), M 10 (middle), and M 22 (bottom). The raw CMDs are cleaned by discarding all stars outside  $2\sigma$  in the color distribution for each bin in the  $m_V$  (see Section 4.2). Each dot represents an object (single stars or unresolved binaries from the catalog). Red and blue dots denote Pop1 and Pop2 stars in each GC following the same definition used in our models (Figure 1; Sections 2.2, 4.2).

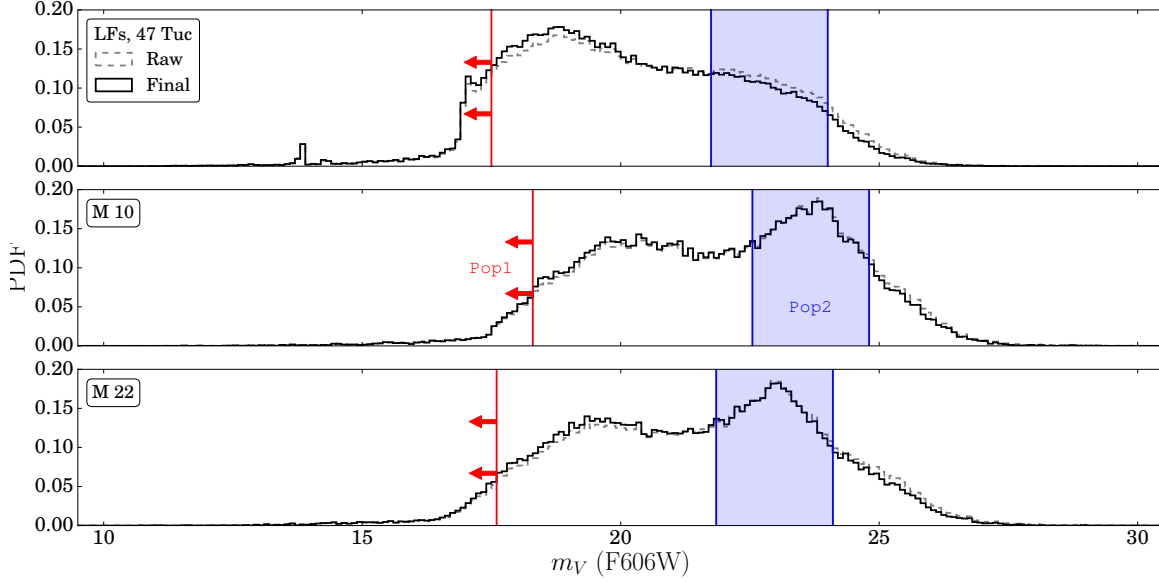


**Figure 6.** Luminosity functions (LF) in the apparent VEGA-mag photometric system corresponding to the raw (dashed) and cleaned (solid) CMDs (Figure 5; Section 4.2) for 47 Tuc (top), M 10 (middle), and M 22 (bottom). Left of the red vertical lines, and the blue shaded region denote the LFs for Pop1 and Pop2 stars. The nearly identical LFs between the raw and cleaned populations, especially in ranges corresponding to Pop1 and Pop2 indicate that our cleanup step did not introduce any significant bias in population selection.

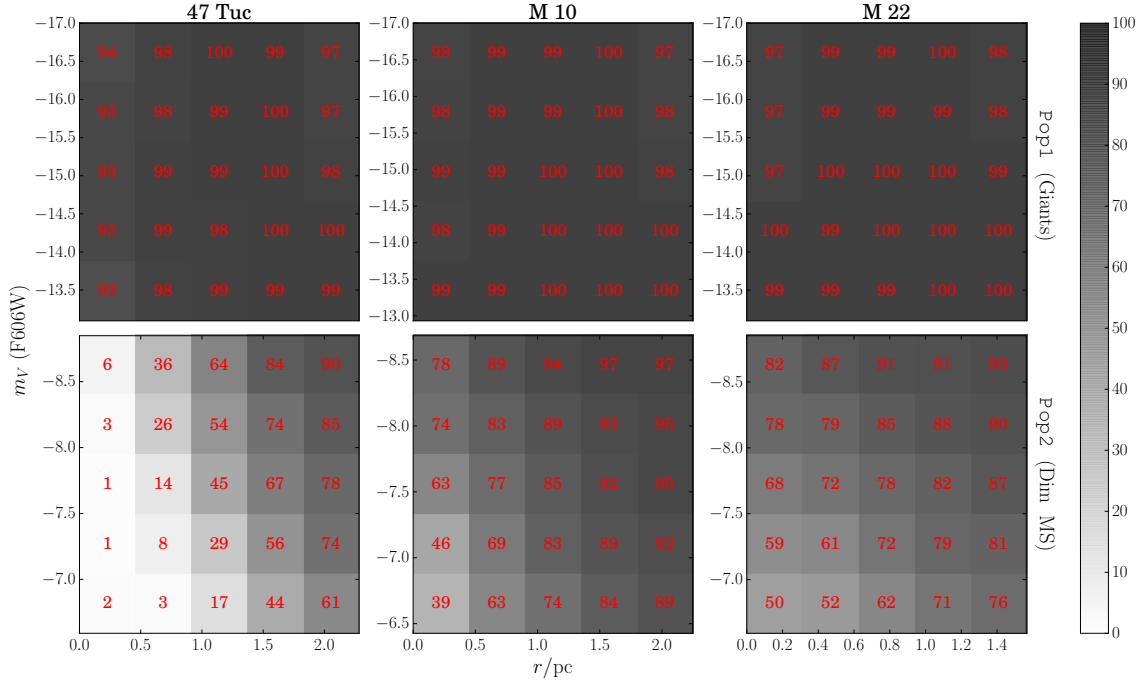


**Figure 7.** Completeness map as a function of the apparent magnitude and cluster-centric radial position for Pop1 (top) and Pop2 (bottom) for 47 Tuc (left), M 10 (middle), and M 22 (right). The completeness fraction is shown in grey-scale. For easy reference, the average completeness fractions are also shown in red in  $5 \times 5$  bins in each panel. As expected, the completeness fraction for giants is nearly 100% in all bins. However, the dimmer low-mass MS stars have much lower completeness fractions, in particular, close to the center of the GCs. The relative completeness fractions are taken into account to debias the calculation of  $\Delta_{r50}$  and  $\Delta_A$  (Section 4.3; Figure 8).

near the center. Difference in completeness can artificially increase the measured  $\Delta$  if not corrected properly. To correct for these biases, we first determine the completeness as a function of magnitude and radial distance using the ACS catalog’s artificial star files (Anderson et al. 2008, see their Section 6 for a full description). In short, Anderson et al. (2008) generate  $10^5$  PSFs of artificial stars drawn from the LF between  $m_v = -17$  and  $-5$  and inject them on top of the raw fields for each cluster, spaced far enough apart to avoid overlap and distributed according to a spatial density that is flat within the core and scales as  $r^{-1}$  outside. They then try to recover the injected artificial stars using the same star-finding procedure from the raw images. If the recovered positions and V,I-band magnitudes are within 0.5 pixel and 0.75 mag of the injected values, they count the stars as successfully ‘recovered’.

We use the radial location  $r$  and magnitude  $m_V$  of all recovered stars to construct a bivariate PDF  $n_{\text{rec}}(r, m_V)$  using a gaussian KDE. Similarly, we create another PDF for all injected stars  $n_{\text{inj}}(r, m_V)$ . The completeness fraction is then simply given by

$$C(r, m_V) = \frac{n_{\text{rec}}(r, m_V)}{n_{\text{inj}}(r, m_V)}. \quad (4)$$

Figure 7 shows the distribution of  $C(r, m_V)$  as a function of  $r$  and  $m_V$  for the relevant range in  $r$  and the two relevant ranges in  $m_V$  for Pop1 and Pop2 stars for all three GCs of interest.

Note that the completeness decreases significantly for Pop2 as  $r$  decreases for all clusters. Completeness for Pop1 stars also shows a similar trend but being bright, they are not affected by crowding as much as the Pop1 stars. To correct for this difference in completeness between the two populations we under-sample the population with higher completeness based on the relative completeness fractions as follows.

We divide the relevant parameter space in  $r$  and  $m_V$  in  $100 \times 100$ , a total of  $10^4$  bins. We calculate the completeness  $C_{i,j}$  at the midpoint of each bin. We then find the minimum in  $C_{i,j}$  and define a probability of sampling as

$$W_{i,j} = \frac{\min(C_{i,j})}{C_{i,j}}. \quad (5)$$

For example, for M 10,  $\min(C_{i,j}) \approx 39\%$  for the Pop2 stars, corresponding to the most centrally located and least bright bin. Stars in a bin with  $C_{i,j} = 99\%$  would then have a probability of selection  $W_{i,j} = 39/99$ .

Using these sampling probabilities, stars are randomly selected from both populations and  $\Delta_{r50}$  and  $\Delta_A$  are calculated using those selected stars. To understand the levels of statistical fluctuations we repeat this exercise 1000 times to obtain distributions for these quantities. This same process is repeated for all three chosen GCs. The mean and standard deviations for these quantities are given in Table 3 for each of these clusters. Figure 8

shows  $\Delta_{r50}$  before and after correcting for completeness – in each case, completeness correction has a large impact. The results are very similar also for  $\Delta_A$ .

## 5. PREDICTING THE NUMBER OF RETAINED BLACK HOLES IN OBSERVED GCs

We now proceed to derive PDFs for  $N_{\text{BH}}$  retained in 47 Tuc, M 10, and M 22, as inferred from the measured  $\Delta_{r50}$  and  $\Delta_A$ . Our numerical models are used to individually calculate  $\Delta_{r50}$  and  $\Delta_A$  using the proper radial limit (Section 4.1) for each cluster. The radial limits used for each individual GC are given in Table 3 for reference. Furthermore, we restrict ourselves to models with  $0.01 \leq Z/Z_\odot \leq 0.25$  in order to be roughly consistent with the low metallicities of the three GCs of interest. We construct individual bivariate distributions for  $\Delta$  and  $N_{\text{BH}}/N_{\text{cluster}}$  from these low- $Z$  models using gaussian KDEs. These distributions are then used to infer the expected number of retained BHs in each GC in the following way.

For each GC we randomly sample  $10^5$  values of  $\Delta_{r50}$  (or  $\Delta_A$ ) from a normal distribution with the mean and standard deviation calculated in Section 4.3. For each of these draws of  $\Delta_{r50}$  (or  $\Delta_A$ ) we randomly sample one value of  $N_{\text{BH}}/N_{\text{cluster}}$  from the bivariate KDE obtained from the models using the appropriate radial limits corresponding to the GC in question requiring that the draw from the KDE has  $\Delta_{r50}$  (or  $\Delta_A$ ) within 1% of the sampled value for the GC. Thus for each observed GC we obtain  $10^5$  values of  $N_{\text{BH}}/N_{\text{cluster}}$  based on the measured  $\Delta_{r50}$  (or  $\Delta_A$ ). We estimate  $N_{\text{BH}}$  by assuming  $M/L = 2$  and that  $N_{\text{cluster}} = M_c/0.5$ , i.e., the average stellar mass is  $0.5 M_\odot$ .<sup>1</sup>

Figure 9 shows the distributions for the predicted retained  $N_{\text{BH}}$  is each GC we analyzed, the actual numbers are also listed in Table 3. The  $N_{\text{BH}}$  distributions for the GCs all have rather large spreads. In all cases the peaks of the distributions are within  $N_{\text{BH}} = 50$ . However, for 47 Tuc and M 22, the maximum  $N_{\text{BH}}$  can be significantly larger, namely,  $\sim 200$  and  $\sim 300$ , respectively. The maximum number of retained BHs in M 10 is a little below  $\sim 100$ . In all three GCs we cannot strictly exclude  $N_{\text{BH}} = 0$ , although, zero retention is outside  $1\sigma$  of the distributions for all three GCs. In fact, it is actually hard to rule out zero retained BHs using a method that tracks dynamical effects such as mass segregation in a cluster since below a certain  $N_{\text{BH}}/N_{\text{cluster}}$  the presence of BHs likely becomes dynamically unimportant. Thus, a sufficiently small number of retained BHs may not be easily distinguishable from zero BHs in a cluster using mass segregation as a probe. Of course,

<sup>1</sup> Of course this assumption can easily be adjusted. The actual quantity calculated is  $N_{\text{BH}}/N_{\text{cluster}}$ . Hence, the keen reader can easily use a better estimate of  $N_{\text{cluster}}$  in future and recalculate  $N_{\text{BH}}$  for each GC. This simply will shift these distributions by a multiplying factor.



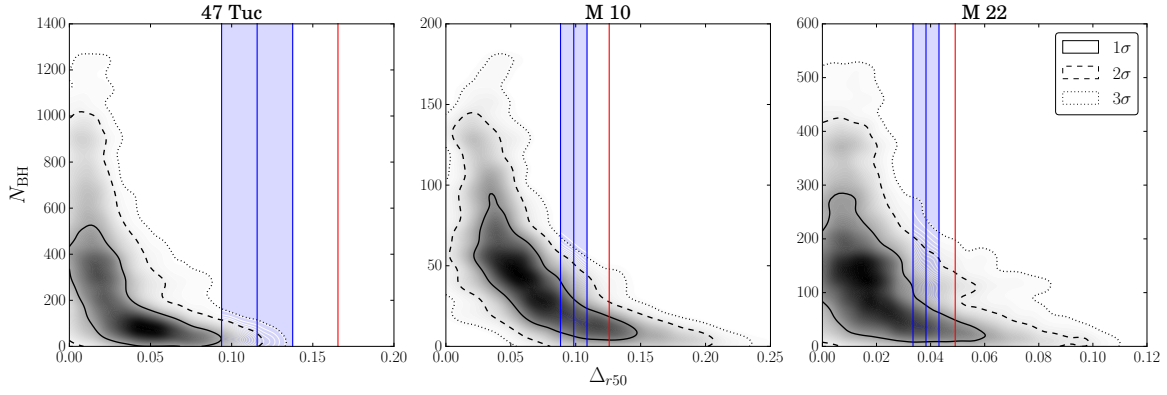


**Figure 8.** Bivariate PDFs for  $N_{\text{BH}}$  vs  $\Delta_{r50}$  for 47 Tuc, M 10, and M 22 from models adjusted using the same limiting radius  $r_{\text{lim}}/r_{\text{hl}}$  as available for the real GCs (see Section 4.1). Black solid, dashed, and dotted contours denote 1, 2, and 3 $\sigma$  for the model PDFs. The vertical blue lines and shaded regions denote the mean and 1 $\sigma$  for the  $\Delta_{r50}$  after all corrections (Section 4). The vertical red lines denote  $\Delta_{r50}$  before completeness correction for reference (Section 4.3). Note that, to remain consistent with the observed metallicities of these GCs only models with  $0.01 \leq Z/Z_{\odot} \leq 0.25Z$  have been used to create the bivariate PDFs from models.

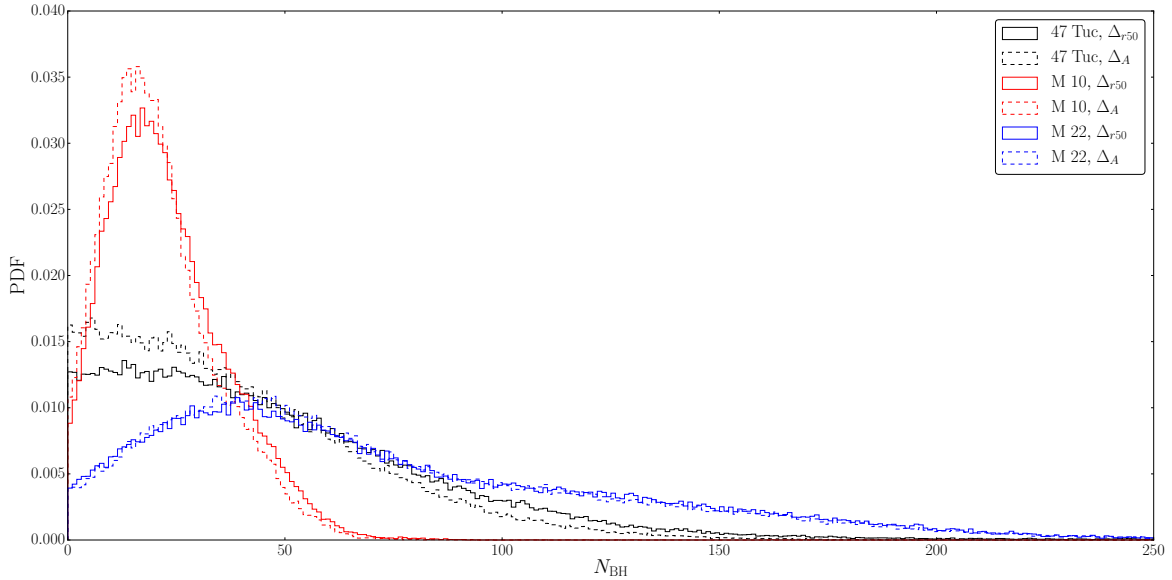


**Figure 9.** Distributions of the retained number of BHs in each GC predicted from the observed levels of mass segregation. Solid and dashed distributions denote distributions obtained using  $\Delta_{r50}$  and  $\Delta_A$ , respectively. Black, red, and blue denote the  $N_{\text{BH}}$  distributions retained in 47 Tuc, M 10, and M 22.

if the candidate BHs discovered in these GCs truly are BHs, then zero retained BHs is excluded by direct observation. Both measures of mass segregation,  $\Delta_{r50}$  and  $\Delta_A$ , give very similar results, while the distributions obtained using  $\Delta_A$  are marginally narrower compared to those obtained using  $\Delta_{r50}$  (Figure 9).

One unavoidable challenge in using this method to predict the retained  $N_{\text{BH}}$  in a GC is of course the availability and quality of data. In particular, the radial limit to which the data exists can in principle be crucial, since the larger the radial limit, the higher should be the measured  $\Delta$  (Section 4.1). While we have mitigated this challenge by limiting our reference model data

also to the same limiting radius, we wanted to test how the quality of these predictions change depending on the adopted radial limits. The ACS survey contains star data to the maximum  $r_{\text{lim}}/r_{\text{hl}}$  for M 10, thus, this M 10 is an ideal GC for a controlled robustness study. While data exists up to  $r_{\text{lim}}/r_{\text{hl}} = 0.9$  for M 10, we repeat the whole process with several smaller  $r_{\text{lim}}/r_{\text{hl}}$  values down to  $r_{\text{lim}}/r_{\text{hl}} = 0.5$ . Reducing the radial extent increases completeness corrections as well as decreases the numbers of member stars in both populations. However, since we have defined the stellar populations in such a way that the member number in each group is typically large, we find that artificially limiting  $r_{\text{lim}}/r_{\text{hl}}$  does not

significantly change our predicted BH numbers for M 10. The peaks of the distributions for  $N_{\text{BH}}$  are very close to each other for all tried  $r_{\text{lim}}/r_{\text{hl}}$ . However, for  $r_{\text{lim}}/r_{\text{hl}} \leq 0.6$  we see a steady increase in the  $1\sigma$  spreads (Table 3). This, together with the similarity in the predicted  $N_{\text{BH}}$  using  $\Delta_A$  or  $\Delta_{r50}$ , bolsters our belief that the predicted retained  $N_{\text{BH}}$  distributions are quite robust.

## 6. SUMMARY

We have presented the general method to indirectly estimate the number of stellar-mass BHs retained in GCs using measurements of mass segregation. While the most reliable estimates would always come from specifically modeling individual clusters, that approach is computationally demanding. Instead, we used realistic models with a wide range in initial properties to determine a general relationship between measures of  $\Delta$  and  $N_{\text{BH}}/N_{\text{cluster}}$  (Section 2). The number of BHs in any given GC can then be determined by measuring  $\Delta$  (following our definitions) and  $N_{\text{cluster}}$  (e.g., adopting a  $M/L$  and average stellar mass) in the GC, making use of the model calibration that connects  $\Delta$  to  $N_{\text{BH}}/N_{\text{cluster}}$ .

We show examples of this process in full detail by estimating the retained  $N_{\text{BH}}$  in three GCs (47 Tuc, M 10, M 22) where candidate BHs have been reported, and where the required data exist as part of the ACS survey for MWGCs. Our analysis carefully takes into account observational constraints such as completeness and the radial extent of the existing data (Section 4). We find that among the three GCs investigated, M 22 contains the highest  $N_{\text{BH}}/N_{\text{cluster}}$  (least mass-segregation), closely followed by M 10 and distantly trailed by 47 Tuc (highest mass-segregation; Section 5; Figure 9). The relative measured values of  $\Delta$  are generally consistent with past analysis of mass segregation in these GCs using very different methods (e.g., Goldsbury et al. 2013). Furthermore, several past studies have shown that the larger the fraction of retained BHs, the larger the observed core radius (e.g., recently Chatterjee et al. 2017b). This trend is reflected in our predicted results as well with M 22 having the largest and 47 Tuc having the smallest  $r_{c,\text{obs}}$  among the three GCs (Table 2). Interestingly, our predicted distribution of  $N_{\text{BH}}$  in M 22 is consistent with the estimated  $N_{\text{BH}}$  by Strader et al. (2012a) based on the two detected candidate BHs, although the latter estimate is based on specific assumptions of the donor type for the detected candidate BHs and expected duty cycles for X-ray binaries (Figure 9, Table 3).

Note that, a central IMBH can also lead to a quenching of mass segregation (e.g., Baumgardt et al. 2004; Trenti et al. 2007; Pasquato et al. 2016). We did not take into account any IMBHs in our models. Theoretically, formation of IMBHs in dense star clusters has been well studied in the past. Their formation requires rather special conditions, such as primordial mass segregation and high initial concentration, which can lead

to runaway stellar collisions before significant cluster expansion due to SN-driven mass loss (e.g., Gürkan et al. 2004; Freitag et al. 2006; Goswami et al. 2012). If this indeed is the formation mechanism for IMBHs, then it is expected that almost all high-mass stars take part in the collisional runaway, leaving little chance to later produce significant numbers of stellar-mass BHs. Even if initial conditions suitable for the onset of a collisional runaway existed in some GC progenitors, it is unclear what actually happens to the massive collision product, i.e., does it grow through repeated collisions and followed by a direct collapse create a massive BH or does severe wind-mass loss limits growth (e.g., Chatterjee et al. 2009; Glebbeek et al. 2009). In any case, based on observed mass segregation, Pasquato et al. (2016) found no suitable candidate IMBH hosts among  $\sim 50$  of the MWGCs they analyzed. Baumgardt (2017) found that apart from  $\omega$ -Cen, no GCs in the MW show evidence of central IMBHs. Further constraints come from radio observations by Strader et al. (2012b), who found no evidence of central IMBHs.

Nevertheless, the dynamical effects of an IMBH and many centrally concentrated stellar-mass BHs of equivalent total mass would be quite similar and are likely indistinguishable using mass segregation alone. Most recently, Kızıltan et al. (2017) suggested that 47 Tuc may contain an IMBH of mass  $2300^{+1500}_{-850} M_{\odot}$  (error bars are  $1\sigma$ ) based on models that contained an IMBH but no stellar-mass BHs. Assuming  $14 M_{\odot}$  as the average BH mass in GCs (guided by our models) we find that the predicted total mass in stellar-mass BHs in 47 Tuc can be up to  $\sim 1500 M_{\odot}$  (up to  $2\sigma$  confidence limit). Given the uncertainties, these numbers are not inconsistent with each other. Thus, the observed pulsar accelerations in 47 Tuc may well be due to the presence of stellar-mass BHs rather than a central IMBH. However, detailed models dedicated for 47 Tuc are necessary to make any strong predictions either way.

In all of the GCs we have considered, the number of retained BHs is typically between  $\sim$  a few tens to  $\sim 100$ . This is likely common for most MWGCs with typical  $r_{c,\text{obs}}$  of up to a few pc. Retained BH fractions are also strongly correlated with the observed core radius (e.g., Chatterjee et al. 2017b). Cluster models that retain  $N_{\text{BH}}$  in excess of  $\sim 10^3$  typically exhibit  $r_{c,\text{obs}}$  that are too large compared to the typical non-core-collapsed MWGCs. We have undertaken a wider survey of all MWGCs contained in the ACS survey catalog to estimate the number of BHs they retain at present. These determinations are expected to be extremely useful for the numerical modeling community since the final  $N_{\text{BH}}/N_{\text{cluster}}$  will likely provide important constraints on the natal kick distributions for the BHs, which lacks either observational or theoretical constraints.

**Table 3.** Predicted Numbers of Retained BHs

Cluster	Radial Limit $r_{\text{lim}}/r_{\text{hl}}$	Population Size		$\Delta_{r50}$ $\pm 1\sigma$	$N_{\text{BH}}$		$\Delta_A$ $\pm 1\sigma$	$N_{\text{BH}}$	
		$N_{\text{Pop1}}$	$N_{\text{Pop2}}$		$\pm 1\sigma$	Max (+2 $\sigma$ )		$\pm 1\sigma$	Max (+2 $\sigma$ )
47 Tuc	0.55	147	616	$0.1157 \pm 0.0219$	$13^{+50}_{-12}$	124	$0.0953 \pm 0.0133$	$8^{+44}_{-7}$	99
M 10	0.9	828	6324	$0.0985 \pm 0.0102$	$17^{+14}_{-12}$	49	$0.0733 \pm 0.0069$	$15^{+13}_{-10}$	46
M 22	0.5	1317	11857	$0.0383 \pm 0.0048$	$39^{+58}_{-34}$	184	$0.0267 \pm 0.0030$	$40^{+53}_{-34}$	180
M 10	0.8	744	5401	$0.0823 \pm 0.0098$	$16^{+13}_{-12}$	49	$0.0634 \pm 0.0064$	$13^{+13}_{-9}$	45
	0.7	660	4454	$0.0613 \pm 0.0095$	$16^{+19}_{-12}$	56	$0.0492 \pm 0.0061$	$14^{+13}_{-11}$	48
	0.6	564	3525	$0.0434 \pm 0.0087$	$16^{+23}_{-12}$	70	$0.0370 \pm 0.0055$	$14^{+15}_{-12}$	54
	0.5	463	2651	$0.0351 \pm 0.0085$	$14^{+25}_{-12}$	72	$0.0257 \pm 0.0051$	$13^{+22}_{-11}$	66

NOTE—Mode and mode-centric  $1\sigma$  are presented for  $N_{\text{BH}}$  for each GC. The ‘Max’  $N_{\text{BH}}$  estimate corresponds to the  $2\sigma$  upper bound for  $N_{\text{BH}}$ . Total mass in BHs can be easily estimated by assuming an average BH mass of  $14 M_{\odot}$ , calculated in our models.

This work was made possible by Northwestern University (NU)’s High-Performance computing cluster *Quest*, on which all CMC models were run. NW acknowledges support from the Illinois Space Grant Consortium, and a grant from NU for summer support. SC acknowledges Hubble Space Telescope Archival research grant HST-AR-14555.001-A (from the Space Telescope Science Institute, which is operated by the Associa-

tion of Universities for Research in Astronomy, Incorporated, under NASA contract NAS5-26555). SC also acknowledges support from CIERA given as a fellowship. FAR acknowledges support from NASA ATP Grant NNX14AP92G and from NSF Grant AST-1716762.

*Software:* CMC (Joshi et al. 2000, 2001; Fregeau et al. 2003; Fregeau & Rasio 2007; Chatterjee et al. 2010; Umbreit et al. 2012; Chatterjee et al. 2013b; Pattabiraman et al. 2013; Rodriguez et al. 2016c).

## REFERENCES

- Abbott, B. P., Abbott, R., Abbott, T. D., et al. 2016a, Physical Review Letters, 116, 061102
- . 2016b, ApJL, 818, L22
- . 2016c, Physical Review X, 6, 041015
- . 2016d, Physical Review Letters, 116, 241103
- . 2017, Physical Review Letters, 118, 221101
- Alessandrini, E., Lanzoni, B., Ferraro, F. R., Miocchi, P., & Vesperini, E. 2016, ApJ, 833, 252
- Anderson, J., Sarajedini, A., Bedin, L. R., et al. 2008, AJ, 135, 2055
- Antonini, F., Chatterjee, S., Rodriguez, C. L., et al. 2016, ApJ, 816, 65
- Askar, A., Szkudlarek, M., Gondek-Rosińska, D., Giersz, M., & Bulik, T. 2017, MNRAS, 464, L36
- Bahramian, A., Heinke, C. O., Tudor, V., et al. 2017, MNRAS, 467, 2199
- Banerjee, S., Baumgardt, H., & Kroupa, P. 2010, MNRAS, 402, 371
- Baumgardt, H. 2017, MNRAS, 464, 2174
- Baumgardt, H., Makino, J., & Ebisuzaki, T. 2004, ApJ, 613, 1143
- Belczynski, K., Bulik, T., Fryer, C. L., et al. 2010, ApJ, 714, 1217
- Breen, P. G., & Heggie, D. C. 2013, MNRAS, 432, 2779
- Chatterjee, S., Fregeau, J. M., Umbreit, S., & Rasio, F. A. 2010, ApJ, 719, 915
- Chatterjee, S., Goswami, S., Umbreit, S., et al. 2009, ArXiv e-prints, arXiv:0911.1483
- Chatterjee, S., Rasio, F. A., Sills, A., & Glebbeek, E. 2013a, ApJ, 777, 106
- Chatterjee, S., Rodriguez, C. L., Kalogera, V., & Rasio, F. A. 2017a, ApJL, 836, L26
- Chatterjee, S., Rodriguez, C. L., & Rasio, F. A. 2017b, ApJ, 834, 68
- Chatterjee, S., Umbreit, S., Fregeau, J. M., & Rasio, F. A. 2013b, MNRAS, 429, 2881
- Chen, X., & Han, Z. 2009, MNRAS, 395, 1822
- Chomiuk, L., Strader, J., Maccarone, T. J., et al. 2013, ApJ, 777, 69
- Dalessandro, E., Ferraro, F. R., Lanzoni, B., et al. 2013, ApJ, 770, 45
- Fregeau, J. M., Gürkan, M. A., Joshi, K. J., & Rasio, F. A. 2003, ApJ, 593, 772
- Fregeau, J. M., & Rasio, F. A. 2007, ApJ, 658, 1047
- Freitag, M., Gürkan, M. A., & Rasio, F. A. 2006, MNRAS, 368, 141
- Fryer, C. L., Belczynski, K., Wiktorowicz, G., et al. 2012, ApJ, 749, 91

- Glebbeeck, E., Gaburov, E., de Mink, S. E., Pols, O. R., & Portegies Zwart, S. F. 2009, *A&A*, 497, 255
- Goldsbury, R., Heyl, J., & Richer, H. 2013, *ApJ*, 778, 57
- Goswami, S., Umbreit, S., Bierbaum, M., & Rasio, F. A. 2012, *ApJ*, 752, 43
- Gürkan, M. A., Freitag, M., & Rasio, F. A. 2004, *ApJ*, 604, 632
- Hansen, C. J., & Kawaler, S. D. 1994, *Stellar Interiors. Physical Principles, Structure, and Evolution.*, 84
- Harris, W. E. 1996, *AJ*, 112, 1487
- Hénon, M. 1971a, *Ap&SS*, 13, 284
- Hénon, M. H. 1971b, *Ap&SS*, 14, 151
- Hurley, J. R., Pols, O. R., & Tout, C. A. 2000, *MNRAS*, 315, 543
- Hurley, J. R., Tout, C. A., & Pols, O. R. 2002, *MNRAS*, 329, 897
- Joshi, K. J., Nave, C. P., & Rasio, F. A. 2001, *ApJ*, 550, 691
- Joshi, K. J., Rasio, F. A., & Portegies Zwart, S. 2000, *ApJ*, 540, 969
- Kalogera, V., King, A. R., & Rasio, F. A. 2004, *ApJL*, 601, L171
- King, I. 1962, *AJ*, 67, 471
- King, I. R. 1966, *AJ*, 71, 64
- King, I. R., Sosin, C., & Cool, A. M. 1995, *ApJL*, 452, L33
- Kızıltan, B., Baumgardt, H., & Loeb, A. 2017, *Nature*, 542, 203
- Kremer, K., Chatterjee, S., Rodriguez, C. L., & Rasio, F. A. 2017, *ArXiv e-prints*, arXiv:1709.05444
- Kroupa, P. 2001, *MNRAS*, 322, 231
- Kulkarni, S. R., Hut, P., & McMillan, S. 1993, *Nature*, 364, 421
- Leigh, N., Sills, A., & Knigge, C. 2007, *ApJ*, 661, 210
- Lombardi, Jr., J. C., Rasio, F. A., & Shapiro, S. L. 1996, *ApJ*, 468, 797
- Lombardi, Jr., J. C., Warren, J. S., Rasio, F. A., Sills, A., & Warren, A. R. 2002, *ApJ*, 568, 939
- Lombardi, C., J. J., Rasio, F. A., & Shapiro, S. L. 1995, *ApJL*, 445, L117
- Maccarone, T. J., Kundu, A., Zepf, S. E., & Rhode, K. L. 2007, *Nature*, 445, 183
- Marín-Franch, A., Aparicio, A., Piotto, G., et al. 2009, *ApJ*, 694, 1498
- Marks, M., & Kroupa, P. 2010, *MNRAS*, 406, 2000
- Miller-Jones, J. C. A., Strader, J., Heinke, C. O., et al. 2015, *MNRAS*, 453, 3918
- Morscher, M., Pattabiraman, B., Rodriguez, C., Rasio, F. A., & Umbreit, S. 2015, *ApJ*, 800, 9
- Morscher, M., Umbreit, S., Farr, W. M., & Rasio, F. A. 2013, *ApJL*, 763, L15
- Pasquato, M., Miocchi, P., Won, S. B., & Lee, Y.-W. 2016, *ApJ*, 823, 135
- Pattabiraman, B., Umbreit, S., Liao, W.-k., et al. 2013, *ApJS*, 204, 15
- Peuten, M., Zocchi, A., Gieles, M., Gualandris, A., & Hénault-Brunet, V. 2016, *MNRAS*, 462, 2333
- Portegies Zwart, S. F., & McMillan, S. L. W. 2000, *ApJL*, 528, L17
- Rodriguez, C. L., Chatterjee, S., & Rasio, F. A. 2016a, *PhRvD*, 93, 084029
- Rodriguez, C. L., Haster, C.-J., Chatterjee, S., Kalogera, V., & Rasio, F. A. 2016b, *ApJL*, 824, L8
- Rodriguez, C. L., Morscher, M., Pattabiraman, B., et al. 2015, *Physical Review Letters*, 115, 051101
- Rodriguez, C. L., Morscher, M., Wang, L., et al. 2016c, *MNRAS*, 463, 2109
- Sarajedini, A., Bedin, L. R., Chaboyer, B., et al. 2007, *AJ*, 133, 1658
- Scheepmaker, R. A., Haas, M. R., Gieles, M., et al. 2007, *A&A*, 469, 925
- Sigurdsson, S., & Hernquist, L. 1993, *Nature*, 364, 423
- Sills, A., Faber, J. A., Lombardi, Jr., J. C., Rasio, F. A., & Warren, A. R. 2001, *ApJ*, 548, 323
- Sills, A., Glebbeek, E., Chatterjee, S., & Rasio, F. A. 2013, *ApJ*, 777, 105
- Sills, A., Lombardi, Jr., J. C., Bailyn, C. D., et al. 1997, *ApJ*, 487, 290
- Sirianni, M., Jee, M. J., Benítez, N., et al. 2005, *PASP*, 117, 1049
- Spitzer, Jr., L. 1969, *ApJL*, 158, L139
- Strader, J. 2014, *A Black Hole in the Galactic Globular Cluster M10*, *Chandra Proposal*, ,
- Strader, J., Chomiuk, L., Maccarone, T. J., Miller-Jones, J. C. A., & Seth, A. C. 2012a, *Nature*, 490, 71
- Strader, J., Chomiuk, L., Maccarone, T. J., et al. 2012b, *ApJL*, 750, L27
- Trenti, M., Ardi, E., Mineshige, S., & Hut, P. 2007, *MNRAS*, 374, 857
- Umbreit, S. 2012, *Nature*, 490, 46
- Umbreit, S., Fregeau, J. M., Chatterjee, S., & Rasio, F. A. 2012, *ApJ*, 750, 31
- Vink, J. S., de Koter, A., & Lamers, H. J. G. L. M. 2001, *A&A*, 369, 574